


Article

Filtering Efficiency and Design Properties of Medical- and Non-Medical-Grade Face Masks: A Multiscale Modeling Approach

Manoochehr Rasekh ^{1,*}, Francesca Pisapia ², Sassan Hafizi ³  and David Rees ¹¹ College of Engineering, Design and Physical Sciences, Brunel University London, Uxbridge UB8 3PH, UK² Newcells Biotech, The Biosphere, Drayman Helix, South St., Newcastle upon Tyne NE4 5BX, UK³ School of Medicine, Pharmacy and Biomedical Sciences, University of Portsmouth, St. Michael's Building, White Swan Road, Portsmouth PO1 2DT, UK

* Correspondence: manoochehr.rasekh@brunel.ac.uk

Abstract: Approved medical face masks have been shown to prevent the spread of respiratory droplets associated with coronavirus transmission in specific settings. The primary goal of this study was to develop a new strategy to assess the filtering and transmissibility properties of medical- and non-medical-grade face masks. In this study, we designed and assessed the filtering efficiency of particles through six different masks with a diverse set of fabrics, textures (woven and non-woven), fiber diameters, and porosity. The filtering and transmissibility properties of face mask layers individually and in combination have been assessed using mathematical analyses and new experimental data. The latter provided velocity profiles and filtration efficiencies for which the data were shown to be predictable. The filtration efficacy and pressure drop across each fabric have been tested using an aerosol particle spray and scanning electron microscopy. To assess clinical significance, the temperature and humidity of the masks were tested on a group of healthy volunteers spanning various age ranges (9–79 years old), utilizing an embedded temperature sensor disc. Also, a mask filter model was developed using fluid dynamic simulations (*Solidworks Flow*) to evaluate the aerodynamic dispersion of respiratory droplets. Overall, the *FFP2* and *FFP3* masks demonstrated the highest filtration efficiencies, each exceeding 90%, a feature of multi-layered masks that is consistent with simulations demonstrating higher filtering efficiencies for small particles (<5 µm). The velocity and temperature simulations of all six masks revealed a low air velocity (~1 m/s) inside the mask and a temperature variation of approximately 3 °C during the breathing cycle.

Keywords: face masks; simulations; analyses; velocity profile; temperature; filtration; particle size

Citation: Rasekh, M.; Pisapia, F.; Hafizi, S.; Rees, D. Filtering Efficiency and Design Properties of Medical- and Non-Medical-Grade Face Masks: A Multiscale Modeling Approach. *Appl. Sci.* **2024**, *14*, 4796. <https://doi.org/10.3390/app14114796>

Academic Editors: Paula Vasquez and Michael Cromer

Received: 30 April 2024

Revised: 25 May 2024

Accepted: 27 May 2024

Published: 1 June 2024



Copyright: © 2024 by the authors. Licensee MDPI, Basel, Switzerland. This article is an open access article distributed under the terms and conditions of the Creative Commons Attribution (CC BY) license (<https://creativecommons.org/licenses/by/4.0/>).

1. Introduction

Approved medical face masks have been shown to prevent the spread of respiratory droplets associated with coronavirus transmission in environments where temperature and humidity each have an important influence. The more effective masks have multiple layers or pleat designs that limit particle penetration [1]. Despite a noticeable variation in particle size, approved face masks have been shown to provide a suitable barrier to infection from external sources [2]. The interactions between humans and their surroundings have promoted the onset of new pathogens with the potential for an epidemic pandemic [3]. Our respiratory system is continually exposed to aerosol nanoparticles (NPs), such as viral or pollutant particles. These airborne particles can have a natural origin (i.e., dust storms, volcanic eruptions), can be man-made (i.e., industrial and car exhaust emissions), or they can be biological microorganisms such as viruses, bacteria, and fungi contained in droplets and aerosols emitted during various expiratory activities such as breathing, talking, coughing, and sneezing [4,5]. Several studies have been conducted to demonstrate the severe impact of inhaling particles on the human respiratory system. They showed that the inhalation

of particles ($<2.5 \mu\text{m}$) caused about 8.9 million deaths in 2015 [6,7]. We have recently experienced the spread of severe acute respiratory syndrome coronavirus 2 (SARS-CoV-2, known as COVID-19), which has led to a significant increase in the number of deaths due to the inhalation of viral particles. As of 12 May 2024, 775,481,326 cases of COVID-19 and 7,049,376 deaths have been reported by the World Health Organization (WHO) [8]. Health agencies across the world have begun to take measures to protect affected communities for population protection, one of which was to contain the spread of COVID-19 among the population through the introduction of personal protective equipment (PPE) such as face masks. Face masks are a useful means by which to mitigate the transmission of diseases, as they protect and preserve the respiratory system of the wearer from airborne particles. Additionally, they protect the wearer, if infected, from spreading the virus. In this way, the risk of both direct and indirect viral exposure can be reduced, and consequently, the probability of infection can decrease [9]. In particular, Hewawaduge et al. (2021) investigated a three-layer mask incorporating copper sulfide (CuS) for inactivating SARS-CoV-2. Their study demonstrated that the mask, with CuS integrated into the outer and middle layers, effectively inactivates the virus within 30 min, achieving near-complete elimination after 1–2 h, and blocking virus-containing droplets efficiently [10]. Also, Zhang et al. (2020) developed spider-web-inspired air filters using a unique electrospinning–netting technique, achieving $>99.995\%$ Particulate matter ($\text{PM}_{0.3}$, the most penetrating particle size $\approx 300 \text{ nm}$) removal, low air resistance, high transparency, and exceptional bioprotective activity for biohazard pathogens [11]. Similarly, Kang et al. (2021) designed a novel face mask filter with an electrostatically rechargeable structure using layer-by-layer electrospun PVDF nanofiber mats on a nylon mesh, enhancing filtration performance and maintaining efficiency under humid conditions [12]. Victor et al. (2021) created a nanocomposite filter media by electrospinning polyvinylidene fluoride (PVDF) blended with varying concentrations of titanium nanotubes (TNTs) between polypropylene nonwoven sheets. This filter demonstrated a bacterial filtration efficiency of 99.88%, indicating its potential for use in facemasks and industrial-scale air filters [13].

During the last few years, scientists have been focused on improving and increasing the filtration efficiency (F), breathability, and comfort of face masks [14]. The two parameters that are used to measure the efficiency of a face mask are (1) filtration efficiency (F), the particle transmission reduction, which reduces the penetration of airborne particles from coming into contact with the wearer, and (2) breathability, which is measured as a pressure drop through the mask [15]. These two factors are combined into a single measure called a filtration quality factor (Q) to assess mask materials [15]. Thus, the efficiency of a face mask would depend on a combination of the particle's size, shape, and charge with the physical properties of the materials used to fabricate the mask, such as the thickness and packing density of fibers, the pore size between the fibers, and the fabric texture (non-woven or woven) [16]. Also, from a fluid mechanics point of view, external factors such as velocity airflow and frequency of respiration have been shown to have an impact on the F of masks [17,18]. Aerosols have different capture mechanisms for preventing penetration through masks. For example, gravity sedimentation, inertial impaction, interception, diffusion, and electrostatic attraction [7,19]. For particles $<1 \mu\text{m}$, the dominant mechanism is still impaction. Diffusion becomes predominant only for particle sizes below the most penetrating particle size (MPPS) (typically in the order of 300 nm) [20]. Konda et al. (2020) have claimed that the flow rate and F of a face mask are inversely proportional to each other. Thus, by increasing the flow rate, the F of a face mask can decrease [21]. A similar conclusion was made by Richardson et al. (2006), who stated that as the flow rate increases, the penetration of particles through the face mask increases [17]. However, filtration efficiency is also dependent on the size of the particles. For instance, the removal of smaller particles is better at low flow rates [22]. In particular, by increasing the airflow velocity, the F of face masks for small particles decreases while increasing for larger particles [23,24]. This phenomenon is due to different mechanisms of particle penetration [25,26]. In addition to this, high flow rates can enlarge the pores in a

material, thus allowing more particles to pass through it. Several studies have compared the F of a range of woven materials, including synthetic (e.g., polyester, nylon) and natural (e.g., cotton, silk) materials, to non-woven materials such as polypropylene, the material that has been used for *FFP3*, *FFP2*, and *Surgical* masks [16,27,28]. Different materials were tested using an automated filter tester (TSI 8130, TSI Inc., Shoreview, MN, USA) at a range of different flow rates (32–85 L/min) to simulate air flow at low and high intensities. The size of the processed NaCl particles was between 0.075 and 0.1 μm since most respiratory viruses such as influenza and SARS-CoV-2 fall in this size range (SARS-CoV-2 virus particles measured about 0.120 μm) [29,30]. Aerosol particles will contain more virus when they are larger than the virus. These studies showed that woven cotton fibers with finer fiber diameter and high porosity have lower F (~20%) and pressure drop (~14 Pa) compared to wider woven cotton fibers with low porosity. However, multi-layered cotton fibers woven to a high density with non-apparent yarn-to-yarn gaps between threads, showed better filtration properties (~26%) than randomly oriented polyester fibers. Although the number of polyester layers increases, the pressure differential increases. Woven silk fibers with larger yarn-to-yarn gaps have shown low F (~5%) and low pressure drop (~7%) [16,27,28].

Melt-blown polypropylene fibers used in *FFP2*, *FFP3*, and *Surgical* masks are layered to form a tangled structure of randomly arranged fibers capable of trapping particles effectively and allowing for good breathability [31]. Typically, ~95% F with ~9 Pa pressure drop is seen for *FFP2* and *FFP3* masks, and ~34% F with ~34 Pa pressure drop is seen for *Surgical* masks.

In the present study, we assessed F (filtration efficiency) for six different masks, including medical- and non-medical-grades with polypropylene, cotton, and silk fibers, composed of a diverse set of fabrics, each with different textures (woven and non-woven), fiber diameters, and porosity. The filtering and transmissibility properties of face mask layers singly and in combination were evaluated using mathematical analysis, providing a velocity profile and F, providing data that were consistent with experimental analyses. These included assessing each mask using SEM for their porosity and sprayed aerosol particles, evaluating (i) their size relative to the mask's porosity, and (ii) the particle distribution applied to the front layer of each mask. The F-measure and pressure drop across each fabric were also assessed using a common aerosol particle spray (Glade[®] aerosol—300 mL, SC Johnson Ltd., Camberley, UK). The humidity, human body temperature (before and during wearing the mask), and the average temperature inside the mask were measured for clinical significance on a diverse group of healthy volunteers aged 9–79 years. Moreover, fluid dynamics simulations were performed using *Solidworks Flow Simulation Software* to assess the aerodynamic dispersion of respiratory droplets and temperature and air flow velocity distributions.

2. Materials and Methods

2.1. Experimental Procedure

2.1.1. Air Flow Velocity Measurement Setup

To measure the filtering efficiency and transmissibility of different face masks, a single layer and a combination of layers were tested. We designed a clear 5 mm-thick acrylic air duct mask container to fit the air flow machine with a rectangular internal area of 10 cm \times 5 cm in two 15 cm lengths on either side, which are clamped and sealed around the mask layer with aluminum clamps. This geometry fits the face mask area more closely than a square or circular profile. At the top end, hooks allowed the attachment of the container to the air flow machine. Polymer tubes were connected to the measurement ends of each pitot tube, and a micromanometer recorded the pressure difference and its velocity conversion (see Figure 1). To prevent leakage, a gasket was clamped around the edges between the container's two halves. A wind tunnel was used to provide a constant air flow rate on the mask surface. The pitot tubes provided velocities at entry and exit, from which the filtration efficiency of each mask was calculated. The analysis was based upon a

maximum central velocity, which was derived from an assumed parabolic velocity profile from the edges to the center of the air duct mask container.

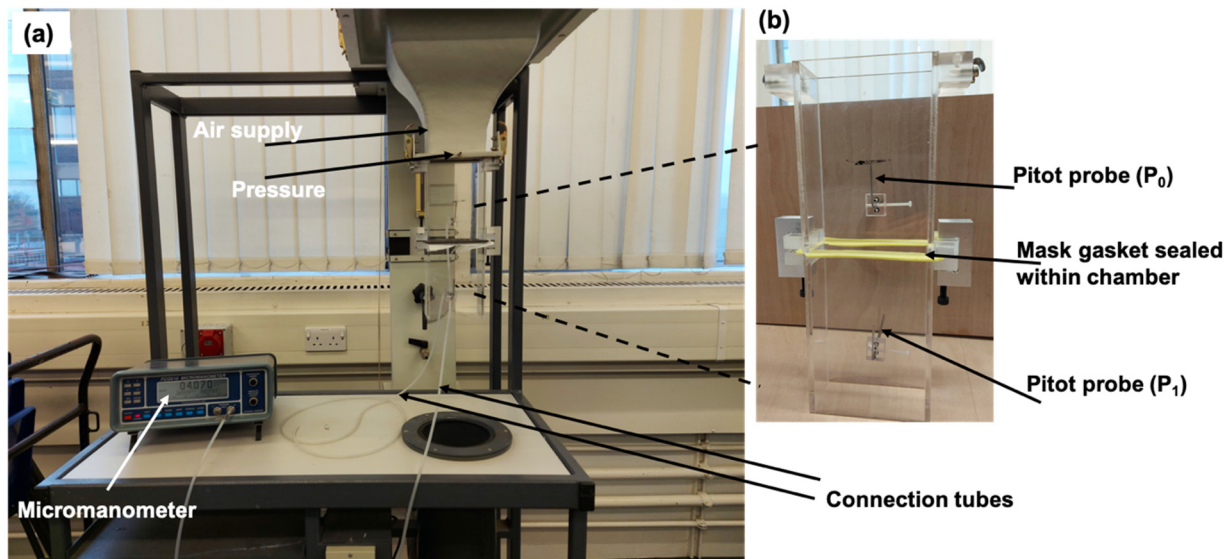


Figure 1. (a) Air flow duct in position within the vertical air flow instrument. (b) Air duct mask container.

2.1.2. Mathematical Analysis

The velocity profile at entry is severe, falling from $v_{(max)}$ at the measuring points to zero at the internal wall surfaces. The mean velocity should be lowered if the wall surface velocity is greater than zero. The mean velocity (v_m) is required to provide a measure of F for individual mask layers. For this, the equation used to describe velocity profiles intersecting at $v_{(max)}$ is given by:

$$v = v_{max} \left(1 - \frac{x^2}{a^2} - \frac{y^2}{b^2} \right) \tag{1}$$

where a and b are the rectangular aperture half-lengths. Base coordinates x and y define the two profiles intersecting at v_{max} . The volume beneath the surface defined by the two profiles is found from a double integral:

$$v = v_{max} \int_{-a}^a \int_{-b}^b \left(1 - \frac{x^2}{a^2} - \frac{y^2}{b^2} \right) dx dy \tag{2}$$

which leads to:

$$v = (4/3) a b v_{max}$$

Equating to a rectangular volume ($2a \times 2b \times v_m$) allows a mean velocity v_m to be found from:

$$(4/3) a b v_{max} = 2a \times 2b \times v_m$$

This gives $v_m = v_{(max)}/3$, where $v_{(max)}$ is a measured entry velocity at the centre of the rectangular area. It will be seen that this simplification of the mean velocity can discriminate between the passage of air through (face velocity) ordered and randomly arranged fibers in wool, silk, and polypropylene materials.

The exit velocity (v_1) is assumed to be uniform given the maximum does not exceed 10.32 (m/s) (v_1); in contrast, the entry velocities (v_0) lay in a narrow range across all masks of 37–39 (m/s). Assuming the parabolic profile in velocity across the central sections, it can be shown:

$$\bar{v}_m = \frac{v_0}{3}$$

given that F (%) is a difference between the velocity at entry and exit and divided by that at entry, expressed as a percentage. Hence, F can be estimated as a percentage using the following formula:

$$F (\%) = [(v_0/3 - v_1)/(v_0/3)] C \times 100$$

where C is an empirical constant that enables the conversion from velocity to filtration efficiency $[(F)\%]$ for a single layer to a whole mask (see the silk example below). Hence, the following formula gives the filtration efficiency of individual mask layers:

$$F (\%) = [1 - (3v_1)/v_0] C \times 100$$

To account for this, a conversion factor (C) has been introduced with the equation above. This assumes that filtration efficiency and velocity difference are proportional. For example, the average filtration efficiency of a single layer of silk was found to be 83%. Since the filtration efficiency of a whole silk mask is 88% [21], therefore, a conversion factor of $C = 0.83$ applies.

Alternatively, as used here, F for the whole mask has been calculated as [23]:

$$F (\text{total}) = 1 - (F_{L1} \times F_{L2} \dots)$$

where, $F_{L1} \times F_{L2} \dots$ is the product of F of individual layers. The usual procedure (ISO, ASTM) for calculating filtration efficiency is based upon the measurement of particle count at entry and exit.

For example, the filtering efficiencies of the three surgical layers are 31, 89, and 50%, respectively (from Table 1); therefore, using the above formula to calculate the $F (\text{total}) = 1 - (0.31 \times 0.89 \times 0.50) = 0.87$ or 87%, which compares well with the experimental data (F whole mask = 88%).

Table 1. The mask layers with their entry and exit velocities and pore sizes.







Mask Types	Mask Layers	V_0 (m/s)	V_1 (m/s)	V (m/s) Calculated	Average Pore Size (μm)	Pictures
Surgical	1st layer	37.76	8.65	36.42	2254	
	2nd layer	38.65	1.31	39.20	180	
	3rd layer	37.61	6.2	36.60	2207	
	Whole mask	38.55	1.56	39.12	1570	
Reusable Cotton	1st layer	38.01	3.78	38.72	4902	
	2nd layer	37.85	5.46	37.96	1056	
	3rd layer	38.60	1.77	39.16	7624	
	4th layer (Filter holder)	38.59	2.56	39.10	7163	
	Whole mask	38.52	1.25	39.18	4936	
FFP2	1st layer	38.21	7.27	37.72	2445	
	2nd layer	37.27	9.57	36.74	4715	
	3rd layer	38.90	1.64	39.39	63	
	4th layer	38.71	1.61	39.39	39	
	5th layer	37.81	9.94	36.40	1221	
	Whole mask	39.02	0.46	39.39	1603	

Table 1. Cont.

Mask Types	Mask Layers	V_0 (m/s)	V_1 (m/s)	V (m/s) Calculated	Average Pore Size (μm)	Pictures
FFP3	1st layer	38.65	5.33	37.96	1746	
	2nd layer	38.28	10.82	36.56	1911	
	3rd layer	38.65	1.82	39.05	265	
	4th layer	38.70	1.80	38.95	46	
	5th layer	38.61	2.15	38.91	89	
	6th layer	37.53	8.20	36.71	1368	
	Whole mask	39.80	0.44	39.35	912	
Antiviral	1st layer	38.61	5.14	38.55	5696	
	2nd layer	38.65	6.45	38.23	608	
	3rd layer	38.55	6.29	38.55	4147	
	Whole mask	38.42	1.75	38.47	3484	
Silk	1st layer	38.50	2.05	39.10	3013	
	2nd layer	38.57	2.28	38.97	3013	
	Whole mask	39.01	1.58	39.18	3013	
Without mask	(control)	34.69	34.69	-	-	

Another example applies to the filtering efficiencies of the six FFP3 layers: 58, 15, 86, 86, 83, and 34%, respectively. Thus, the above formula can be used to calculate the F (total) = $1 - (0.58 \times 0.15 \times 0.86 \times 0.86 \times 0.83 \times 0.34) = 0.98$, or 98%, which again compares well with the experimental data (F whole mask = 97%). The analysis is based on the assumption of the existence of the maximum central velocity within the air duct mask container. This measure provides a convenient comparison of each mask's performance.

2.1.3. Pressure/Velocity Measurement

A microprocessor-based precision instrument used for measuring ultra-low-range differential pressures (Micromanometer, FC0510, Nottingham, UK) was calibrated and used to convert from pressure to velocity at the entry ($p_0 \rightarrow v_0$) and exit ($p_1 \rightarrow v_1$) positions. For this, pitot probes were installed within the in-house-designed air duct mask container.

Velocity Measurement Using Pitot Tubes

Two pitot probes were positioned centrally in the container's rectangular area at a distance of 15 cm apart, with the tip of each probe (entry and exit) on either side of the clamped mask being 7.5 cm. The formula used for conversion from pressure to velocity is shown below [32]:

$$V = [2(p_0 - p_1)/\rho]^{1/2}$$

where $\rho = 1.204 \text{ kg/m}^3$ is the density of air at 20°C under atmospheric pressure. This allowed for the entry velocity (v_0) to be provided directly by the measurement instrument, the micromanometer (Figure 1). The manometer calculated the velocity and pressure directly from the equation above. The air flow velocity at the centre and edges was measured with a pitot tube at each position. This confirmed the parabolic distribution employed in the theory.

2.1.4. Particle Aerosol Spray

Glade aerosol particles ($0.05\text{--}1 \mu\text{m}$) were applied at a distance of 60 cm onto the front layer of six different masks for 10 s. The samples were left to dry before the scanning

electron microscopy (SEM) analysis, in which they were mounted for measurement of particle size, pore size, and their distributions. This was to establish the particle size relative to the pore size and thereby assess the transmissibility and filtering efficiency of each mask. Each mask to be sprayed was sealed within the acrylic duct container and then attached to the wind tunnel device. No further handling occurred prior to testing (Figure 1).

2.1.5. Mask Temperature Sensor

Two samples (*Surgical* and *FFP3* masks) were used to measure the body temperature within the mask layer in normal use as a protective cover. For this, the Tempo Disk temperature sensor (version 8.7) was used to measure the body temperature, and a non-contact clinical thermometer (EmsiG GmbH Co, CT95, Humburg, Germany) was used to measure human body temperature in the region between the mouth and the mask interior. The Tempo Disk was calibrated in the laboratory at room temperature. The temperature and humidity were measured in twelve volunteers (ages 9–79 years) during their normal daily activities for two different masks, the *Surgical* and *FFP3*, over a period of 30 min (six consecutive readings, 5 min apart). These provided representative temperature and humidity profiles associated with breathing (inhale and exhale transmission). Thus, these measurements would assess the masks' F values by establishing variations in temperature and humidity throughout continuous use.

2.1.6. SEM Analysis of Mask Surfaces Sprayed with Micro-Particles

Scanning electron microscopy (SEM) was carried out using a JOEL instrument (JSM IT200, Tokyo, Japan). SEM was operated at an accelerating voltage of 10 kV to study size and surface morphology. The aerosol-sprayed particles (0.05 to 1 μm) on each face mask were observed using the SEM microscopy in low vacuum mode at an operating pressure of 50 Pa. For this purpose, the six different face masks (*Surgical*, *Reusable Cotton*, *FFP2*, *FFP3*, *Antiviral*, and *Silk*) were used and assessed for their particle size and morphology and their relative comparison at varying magnifications between 1000 and 5000. The whole mask's layer was carbon-coated to a thickness of ~ 10 nm before SEM analysis.

2.2. Mask Filter Model

Fluid dynamics simulations were performed using *Solidworks Flow Simulation* software, version SP0, 2022 (Dassault Systems, France) as a preliminary model study. The finite element analysis was also performed for a mesh study using *Solidworks* software, version SP0, 2022; we considered a standard fit of the mask to the mannequin's head. A small leaking gap around the chin area was taken into consideration. However, previous studies show that for particles greater than 100 nm, there is no strong relationship between leakage and particle size; on the other hand, particles below 100 nm were observed at low flow rates [18,33]. Gravity was included in the study along the z-axis in the negative direction (-9.81 m/s^2). Air and water were considered fluids for the analysis.

During the simulation, no change in the water phase was assumed. Based on previous studies [34,35], the ambient air composition was set to 0.03% CO_2 , 20.71% O_2 , 1.23% H_2O , and 78.03% N_2 ; a turbulent flow type was selected. As a boundary condition, an inlet velocity flow was added based on the data provided in Table 1 in order to simulate someone without a mask breathing from a distance of 50 cm from the source. The engineering database within *Solidworks* was utilized to configure the porosity of the face masks. Porous material was selected from the drop-down menu, and the porosity was determined based on the data provided in Table 1 below. Goals were set to monitor the velocity on both the mask and on the face of the wearer. The computational domain was reduced in order to reduce the processing time.

Temperature and Velocity Simulations

To study the air flow velocities and temperature distributions within six different face masks, computational fluid dynamics (CFD) simulations were carried out using

Solidworks software (SP2.0, 2022; Dassault Systems, Paris, France). The physical domain (mannequin head with face mask used for simulation) was designed before the simulations. Air was chosen as the working fluid for the simulations. Gravity was applied along the z-axis direction (-9.81 m/s^2). The RNG k- ϵ turbulence model was used to simulate turbulent airflow. The k-epsilon turbulence model is a mathematical model used to simulate turbulence airflow conditions, while the sinusoidal breathing cycle has been defined by using a sinusoidal function. An inlet volume flux rate of 0.5 L/s was considered the boundary condition. The pore sizes of the six different masks were used to simulate air flow penetration. For this, the measured pore sizes have been added to reproduce the porosity of different face masks. As a result, the air passing through the mask will experience friction and, therefore, flow resistance due to the presence of pores in the mask. The different porosities were simulated using the engineering database available on *Solidworks*. A Quad/Tri mesh type was generated to ensure the accuracy of the results. Moreover, this mesh type generates a mesh density capable of analyzing the flow through the thickness of the mask. Controlled temperature and air flow velocity distributions were applied at the boundary. The transparent feature was applied to the face masks in order to analyze the air flow velocity and temperature distribution. The face velocity is defined as the ratio between the flow rate and the area of the filter. Since we considered the face mask as the final surface to conduct our analysis, the velocity obtained in our work from the simulations is the face velocity.

2.3. Materials

Six medical and non-medical face masks were obtained from recognized suppliers. They included the medical-grade IIR *Surgical*; *Reusable Cotton*; *Antiviral* face mask; pure mulberry folded *Silk*; and filtering face pieces 2 and 3 (*FFP2* and *FFP3*). The former is a N95 equivalent, and the latter is a certified N99.

3. Results and Discussion

Figure 1a shows the arrangement for the pressure and velocity measurements made in the manner described above. The air duct was designed and sealed around the mask, positioned transversely at its centre (mask gasket sealed within the chamber). Pitot tubes, central to the air flow, were positioned at 7.5 cm on either side (see inset Figure 1b). In order to prevent leakage, each mask layer was sealed with a clamped rectangular gasket rim.

Figure 2a–f show SEM micrographs displaying porosity in both woven and random fiber structures. Pores lie between the cross weave and within overlaying fibers with random orientations. Figure 2a,c,d are randomly orientated fibers, and Figure 2b,e,f are woven or ordered fabrics. The average pore sizes vary within the different mask layers, as indicated in Table 1. Further structural details have been reported earlier by Rasekh et al. (2022) [36].

Figure 2g,h show the relative pore size and fiber diameter of the mask's constituents based upon SEM measurements. Each SEM image shows the texture as an ordered weave or random overlay of fine fibers, revealing porosity and fiber diameter. Clearly, *Reusable Cotton* has the largest and *FFP3* has the lowest pore size, whereas *Antiviral* with *Silk*, and *Surgical* with *FFP2* showed comparable pore sizes. Fiber diameters lay in a narrow range, with the largest and smallest applying to *Surgical* and *Silk*, respectively [36].

Table 1 shows the velocities measured at entry and exit at 7.5 cm away from either side of the whole masks and their individual layers. The layers were clamped and sealed within the two halves of the air duct mask container. Filtering efficiency was calculated from the average reduction velocity between the two measurement positions using the following equation: $[(v_0 - v_1)/v_0]$, where v_0 is the average velocity within the profile that increases from zero at the air duct interior surfaces to the maximum at the central measurement point. The v_0 and v_1 were taken from the micromanometer measurement for the mask's layers and the whole mask. The final V was calculated from the equation in Section 2.1.3, "velocity measurement using pitot tubes".

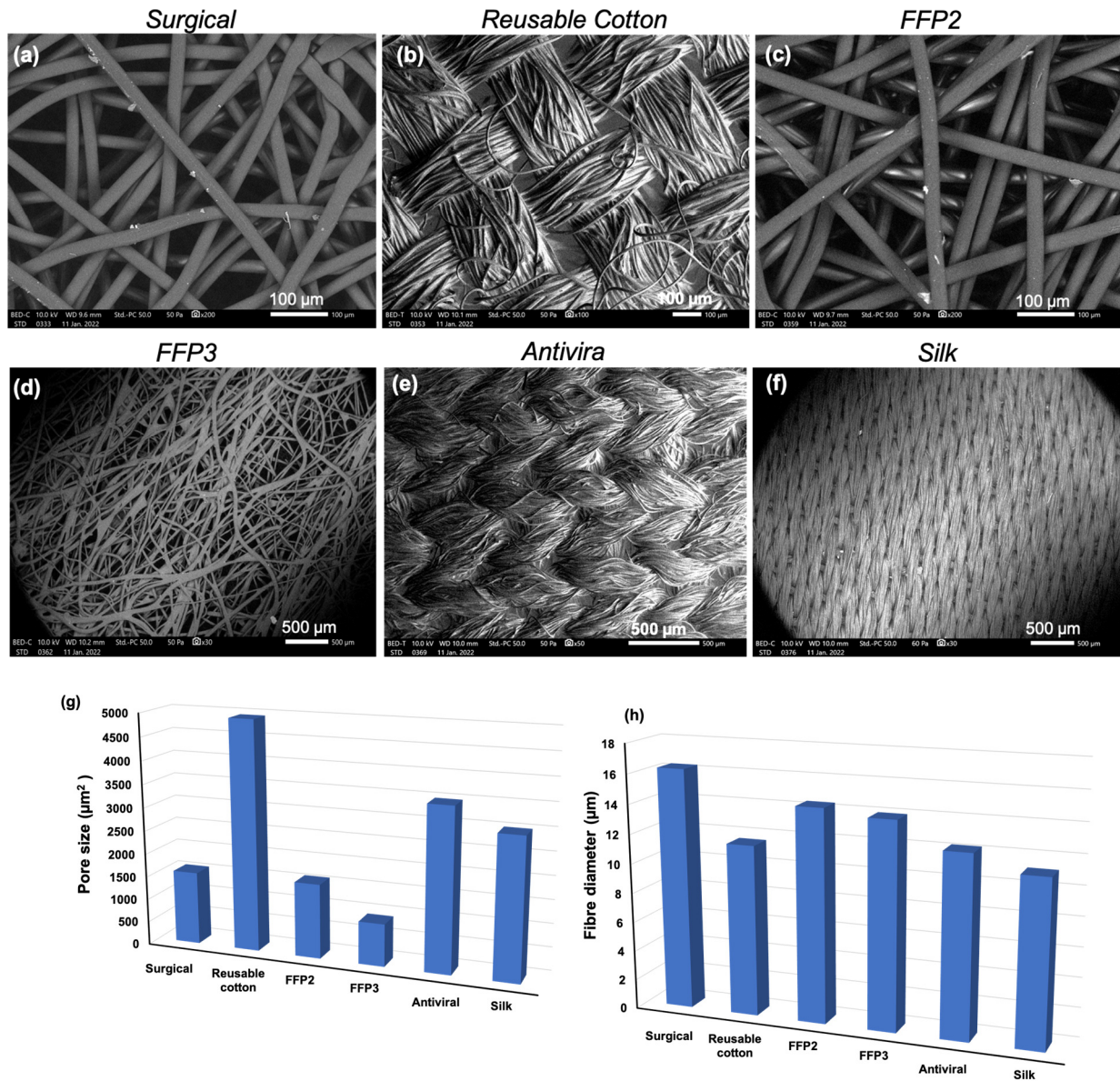


Figure 2. SEM images of six different mask surfaces. (a,c,d) Surgical, FFP2, and FFP3 with randomly orientated fibers. (b,e,f) Reusable cotton, antiviral, and silk with woven or ordered fabrics. (g,h) Graph showing the pore sizes and fiber diameters of masks.

An average velocity (\bar{v}) for this profile was taken to be 1/3 of the peak measured value. Also, Table 1 shows the average pore size for individual masks' layers as well as for the whole mask. These are to be compared with the droplet size ranges, from 1 µm to 10 µm, observed in the magnified images from the SEM of aerosol-sprayed surface particles (Figure 3).

Generally, the greater the pore size of a layer, the greater is the exit velocity (v_1). The calculated velocities in Table 1 were checked by a second calibrated instrument providing velocities v_0 and v_1 directly. The 15-cm separation between the pitot tubes at positions 0 and 1 amounted to a negligible contribution to the potential energy exchange ($2g \times (\Delta h) = 2.943 \text{ m}^2/\text{s}^2$).

Also, Figure 3 shows the micro-particle distribution from an aerosol spray at magnification indicated for *Surgical* (a,b), *Reusable Cotton* (c,d), *FFP2* (e,f), *FFP3* (g,h), *Antiviral* (i,j), and *Silk* (k,l) masks. Some particles appear dispersed in Figure 3(a,e,i) while others have combined to a larger size (Figure 3(b,f,j)). Dispersion among the multiple cotton fibers

appears in Figure 3c,g,k and on a single fiber in Figure 3(d,h,l). The random orientation of non-woven fibers (*Surgical*, *FFP2*, and *FFP3*) allows passage of small-size particles more easily than the ordered woven fabrics (*Reusable Cotton*, *Antiviral*, and *Silk*). Micro-particle deposition is important to consider in reusable face masks, and therefore washing instructions should be followed carefully. However, over washing can damage the fabric, so the manufacturer's end-of-life instructions should be followed. The spray is an aerosol mist of liquid with a size range of $0.05\ \mu\text{m}$ to $1\ \mu\text{m}$, giving a polydisperse distribution of particles. The pore size allows small particles to penetrate the mask; larger particles deposited upon the mask surface, as shown in (Figure 3(a–l)).

Figure 3m displays the velocity of each mask and of its layers in bar chart form. For this, an average velocity at entry was required for the three-dimensional velocity profile over the rectangular duct area. The maximum entry velocity (v_1) at the air duct mid-position is shown. For each mask, the first velocity bar displayed is that for the whole mask, followed by bars representing the individual layers. Overall, the results show that the filtration efficiencies of multi-layered masks are greater than those of their individual layers. The comparison between the exit velocities (m/s) of each whole mask is as follows: *FFP3* (0.4 m/s) and *FFP2* (0.5 m/s) have the greatest values, whereas the lowest is that of the *Antiviral* mask (1.8 m/s). The *Surgical* and *Silk* masks have similar exit velocities (1.6 m/s), and the *Reusable Cotton* exit velocity is slightly lower at 1.3 m/s. This indicates that the greatest filtering efficiency applies at the lowest exit velocity (see Figure 3m and Table 1).

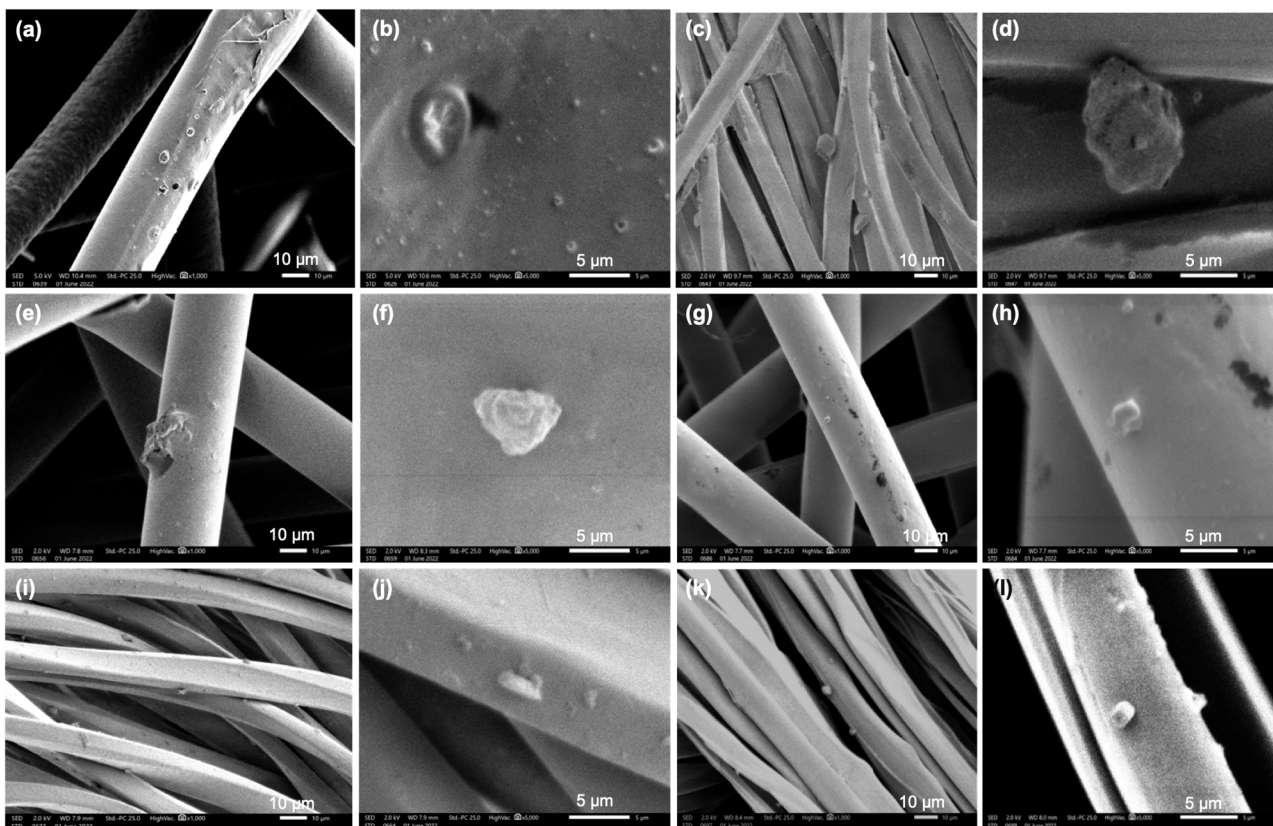


Figure 3. Cont.

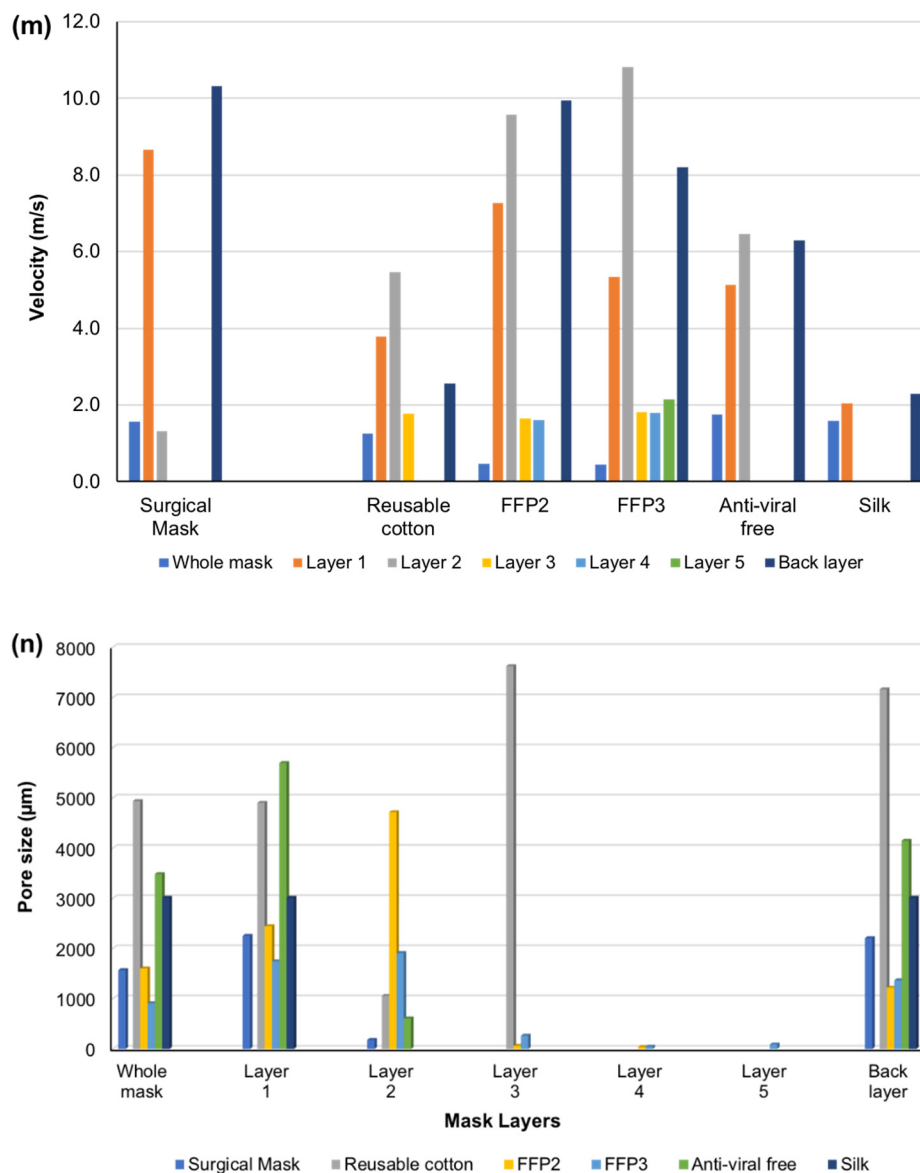


Figure 3. The sprayed aerosol micro-particles on the outside layer of: (a,b) Surgical; (c,d) Reusable Cotton; (e,f) FFP2; (g,h) FFP3; (i,j) Antiviral; (k,l) Silk masks. (m,n) Graphs show the exit velocity of whole and individual layers (m); and the pore size of whole and individual layers (n).

Figure 3n demonstrates the average pore size of each mask as a whole and for its individual layers. The first block of bars applies to the six whole masks, followed by individual layers depicted by the color key. As whole masks, the *FFP3* was the least porous (912 µm), whereas the *Reusable Cotton* was the most porous (4936 µm).

As an example, $v_0 = 37.76$, $v_1 = 8.65$ (m/s), and $F = 31\%$. These values for the first layer of the *surgical* mask are judged to be a realistic estimate of the passage of air (face velocity) through a porous face mask layer. An estimate of the total area of the pores based upon the SEM analysis is assumed to be distributed evenly as an average calculation within the air duct rectangular area. Here, the average porosity (pore size) of each layer of six different masks and of each whole mask was calculated and is shown in Table 1. These averages lie in a range of 2.5–24% of the average value of between five to fifteen SEM measurements, which are shown in the bar chart (see Figure 3n) [36].

Figure 4 is a mesh study of a surgical face mask, showing the three different mesh zones (mask, mannequin head, and exterior) for the convergence of the results. This phenomenon is due to the mask's structure. To conclude, according to the simulations,

the masks with the highest filtering capabilities for particles ($<5 \mu\text{m}$) are *FFP3* and *FFP2*. This is substantiated by the direct measurement of pore size and fiber diameter given in Figure 2. These findings confirmed earlier studies on mask layer transmissibility [1].

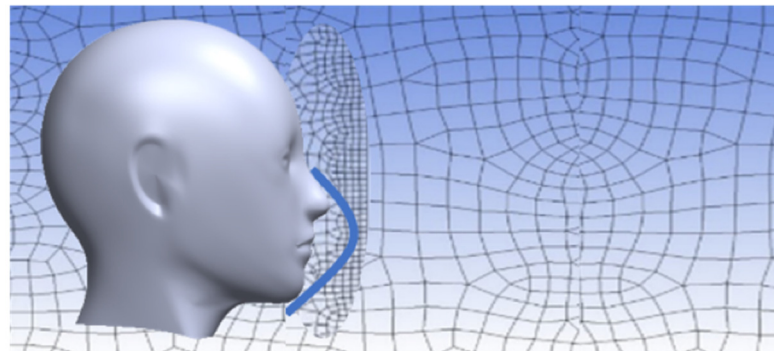


Figure 4. Mesh study using finite element analysis (the blue line represents the face mask profile).

The volume fraction of water is used to evaluate the water permeability of the six different face masks. Figure 5a–f show the velocity profile distribution from the source to the wearer along the horizontal y-axis. The velocity in the proximity of the wearer’s face is reduced drastically. The droplets represent the water distribution within the flow.

The size of the droplets was set to $5 \mu\text{m}$ according to the present results and previous studies [37,38]. Different analyses were used in series in order to evaluate which mask reduces better the volume fraction of H_2O at the wearer’s face.

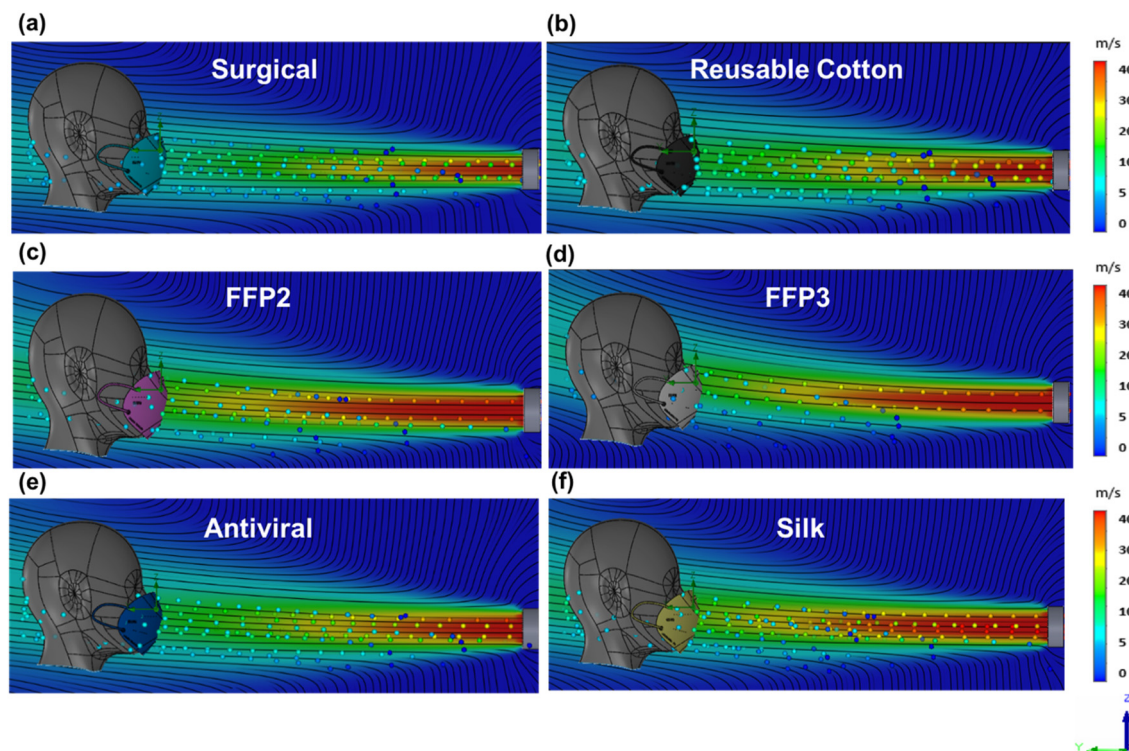


Figure 5. CFD simulations showing the velocity profile and the droplets size distribution from the source to the wearer while wearing masks. (a) Surgical (light blue). (b) Reusable cotton (black). (c) FFP2 (purple). (d) FFP3 (grey). (e) Antiviral (dark blue). (f) Silk (yellow).

The performance of the masks was determined by evaluating the volume fraction of water at the wearer’s face (water penetration per unit volume of mask). Figure 5d shows

that the droplet's cloud at the *FFP3* mask surface is less dense, and therefore, as shown in Figure 6, the volume fraction of water on the mask surface is low, as the *F* calculation shows (Table 2). This means that the *FFP3* mask protects the wearer by filtering the majority of the particles. A similar result is shown in Figure 5c for the *FFP2* mask. The droplet's cloud around the mask surface is sparse, meaning that the volume fraction of water at the mask surface is low (Figure 6). This means that the *FFP2* mask is capable of blocking and filtering most of the airborne particles. In the surgical mask, the droplet cloud around the mask appears to be denser than the cloud near the *FFP3* and *FFP2* masks (Figure 5a). In fact, Figure 6 shows that the volume fraction of water near the *Surgical* masks is higher than the cloud near the other masks. However, while not as effective as the *FFP2* and *FFP3* masks, the *Surgical* mask is still capable of protecting the wearer from airborne particles. Surprisingly, the *Reusable Cotton* mask can filter most of the 5 μm particles contained in the air flow emitted from the source (Figure 5b).

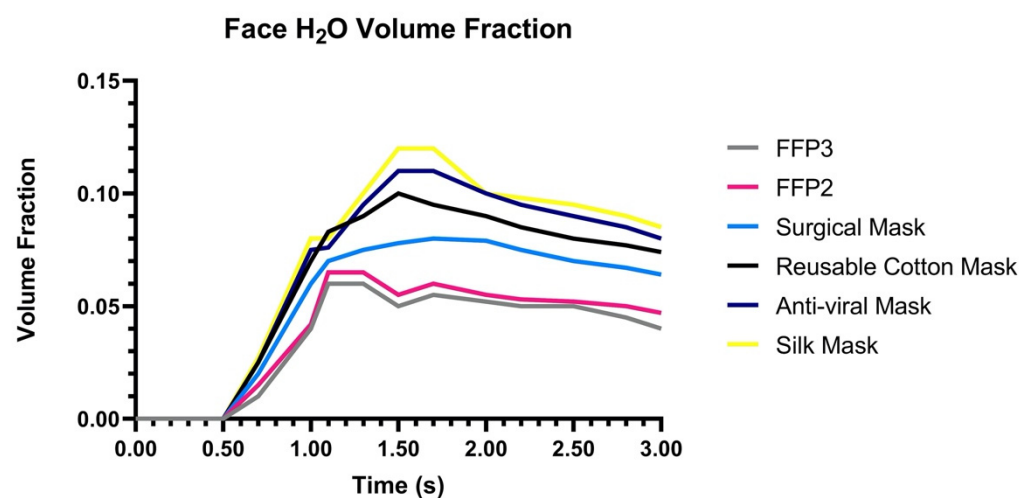


Figure 6. The plot shows the different volume fractions of H₂O at the wearer's face when wearing different masks.

In fact, as shown in the graph in Figure 6, the volume fraction of water on the surface of the *Reusable Cotton* mask is greater than the fraction present on the other face masks but close to the volume fraction present on the surface of the *Surgical* mask. Finally, the *Antiviral* and the *Silk* masks show similar behavior (Figure 5e,f). The droplet cloud around the masks is very dense, meaning that both masks do not have adequate protection against airborne particles. In fact, the volume fraction of water on both mask surfaces is significantly higher compared to the volume fraction of water on all the other mask surfaces. Also, the simulation shows that the volume fraction of water when wearing a *FFP3* mask drops significantly compared to the other five masks (Figure 6 (grey graph)).

Table 2. Measured filtration efficiencies of the whole versions of each mask.

Mask Type	V_0 (m/s)	V_1 (m/s)	Filtration Efficiency (F Total) %
Medical-grade IIR Surgical	38.55	1.56	88
Reusable cotton	38.52	1.25	90
FFP2	39.02	0.46	96
FFP3	39.80	0.44	97
Antiviral	38.42	1.75	86
Silk	39.01	1.58	88
Without mask (Control)	34.69	34.69	0

3.1. Interactive Temperature and Humidity Influences

Another potential benefit for wearers of masks is that the humidity created within the mask may help combat respiratory diseases such as COVID-19. The scientists in the national institute of diabetes and digestive and kidney diseases at the National Institutes of Health (NIH) found that wearing a face mask can significantly increase the humidity in the air that a mask-wearer breathes in (inhaled air). As hydration of the respiratory tract can benefit the immune system, this has been linked to lower disease severity in people infected with SARS-CoV-2 [39]. A high level of humidity could limit the spread of viruses to the lungs by stimulating mucociliary clearance (MCC), which is the primary innate defense mechanism of the lung for removing mucus and harmful particles. Also, a high level of humidity can strengthen the immune system through the secretion of immune signaling proteins such as interferons, which can regulate the fight against viruses [40]. In contrast, a low level of humidity could impair MCC and the interferon response, which is thought to be one of the reasons why respiratory infections are transmitted especially widely during cold weather [39].

To investigate this further, a study examined *Surgical* and *FFP3* masks for these factors. Temperature and humidity were measured for twelve volunteers over 30 min, with six consecutive readings taken every 5 min, using a Tempo Disk temperature sensor placed inside each mask. The body temperature of volunteers was also measured using a non-contact clinical thermometer before and after wearing the masks to assess the effect of the masks. The results showed that both *Surgical* and *FFP3* masks increased the level of humidity in inhaled air, but to varying degrees depending upon the wearer's age. Nevertheless, as mentioned earlier, the rise in humidity within the mask may enhance the immune system by triggering the secretion of immune signaling proteins, such as interferons, which could contribute to combating respiratory diseases (see Table 3) [39,40].

Table 3. Measurements of in-mask humidity and temperature, as well as body temperature in volunteers wearing surgical ($n = 8$) and FFP3 ($n = 4$) masks.

Mask Type	Average Temperature (Inside Mask) °C	Humidity (Inside Mask) %	Body Temperature (before Wearing Mask) °C	Body Temperature (While Wearing Mask) °C
Surgical	28.9	79.6	36.5	36.8
Surgical	29.0	91.9	37.0	37.0
Surgical	31.4	71.3	36.9	37.1
Surgical	29.7	98.6	36.6	36.6
Surgical	28.8	82.3	36.3	36.4
Surgical	29.4	95.1	36.6	36.7
Surgical	31.0	91.2	36.8	37.1
Surgical	29.2	83.0	36.0	36.5
FFP3	31.6	91.0	36.8	37.0
FFP3	30.3	75.0	36.8	36.7
FFP3	31.0	70.1	36.5	36.6
FFP3	31.6	79.4	35.8	36.2

The temperature inside the masks was also found to be higher compared to room temperature (21–23 °C). The results also reveal that changes in body temperature while wearing the masks are not clinically significant. This experiment therefore demonstrated that humidity changes occur more rapidly than temperature changes as a result of wearing the masks, even for short durations. Furthermore, in-mask temperature appears to be closely associated with exhaled breath temperature, which can be linked to lung inflammation [41].

The evaluation of exhaled breath temperature could provide a useful way to evaluate the effectiveness of medical and non-medical mask grades and to detect pathological processes in the respiratory system. An assumed mechanism will be based on changes in the blood flow in the conduction airways. This would reveal different disease states, which influence the temperature of exhaled gases. To prove this concept, fractional exhaled nitric oxide (FeNO) has been measured using an open-circuit, single-breath method in a closed indoor environment [42]. This evaluation demonstrated associations between exhaled breath temperature and bronchial blood flow, FeNO, and sputum cellular content. Further studies using this method using portable hand-held devices and introducing multiple breathing modes offered practical applicability and showed less dependence on temperature. Therefore, the potential application of exhaled breath temperature evaluations has been explored for the monitoring and diagnosis of airway diseases in clinical practice [42].

3.2. Temperature and Velocity Simulations

Temperature and air flow velocity distributions have been analyzed during normal breathing conditions while wearing the six different masks. For this study, a maximum breathing flow rate of 0.5 L/s was considered the initial inlet condition based on previous studies [43,44]. The breathing cycle is described by a time-dependent, unsteady flow rate profile. The governing equation for unsteady and incompressible turbulent flow was used (the RNG $k-\varepsilon$ turbulence model) to simulate the breathing cycle, as used by other scientists [43–48]. The no-slip boundary condition was set at the mouth, nose, and forehead of the face mask wearer. The external/ambient temperature was set to 23 °C. The initial temperature inside the mask was set at 31.2 °C based on the average data obtained from the 12 volunteers (Table 3).

The pore size of the masks was measured and used based on our previous study [36] to simulate the air flow resistance. The material properties were selected from the engineering database available on Solidworks. The velocity inlet follows the velocity profile shown in Figure 7, with a direction normal to the boundary and a turbulent intensity of 1%. The turbulent kinetic energy was set to $10^{-5} \text{ m}^2/\text{s}^2$, and the turbulent dissipation rate was set to $10^{-6} \text{ m}^2/\text{s}^3$ in order to conduct the equation within the software and simulate the air flow through the mask to demonstrate the air flow and temperature distributions [49,50]. A duration of five respiratory cycles was used to simulate with a time step of 0.1 s. The largest velocity during exhalation and inhalation was observed at 2.4 m/s and 1.35 m/s, respectively. The velocities outside the masks were relatively small compared to the velocities at the forehead and nose. The flow velocities became larger during exhalation and inhalation under the nostrils, which can be due to the small distances between the nostril and the upper part and between the upper and lower parts of the mask.

The air flow velocity distribution results inside the face mask wearer during the inhalation peak ($t_2 = 3 \text{ s}$) and the exhalation peak ($t_1 = 1 \text{ s}$) are shown in Figure 7. Overall, air flow velocities were higher inside the mask compared to outside for both inhalation and exhalation. During the inhalation phase (Figure 7a,c,e,g,i,k), all six face masks showed a low air velocity distribution ($\sim 0.8\text{--}1.4 \text{ m/s}$) inside the mask (within the nose and mouth). The *Silk* and *Antiviral* masks had a higher air flow velocity (2.3 m/s) around the mouth. However, during the exhalation phase, the air flow velocity was distributed evenly inside the *FFP3*, *FFP2*, and *Surgical* masks (Figure 7b,d,f), whereas the air flow velocity was higher for the *silk* (Figure 7j) and *antiviral* (Figure 7l) face masks. Moreover, it can be observed that during the exhalation phase, more air passes through the *Silk* and the *Antiviral* masks (blue areas in Figure 7j,l). These results correlate with the high pore size and low filtration efficiencies measured for the *Silk* and *Antiviral* face masks [33].

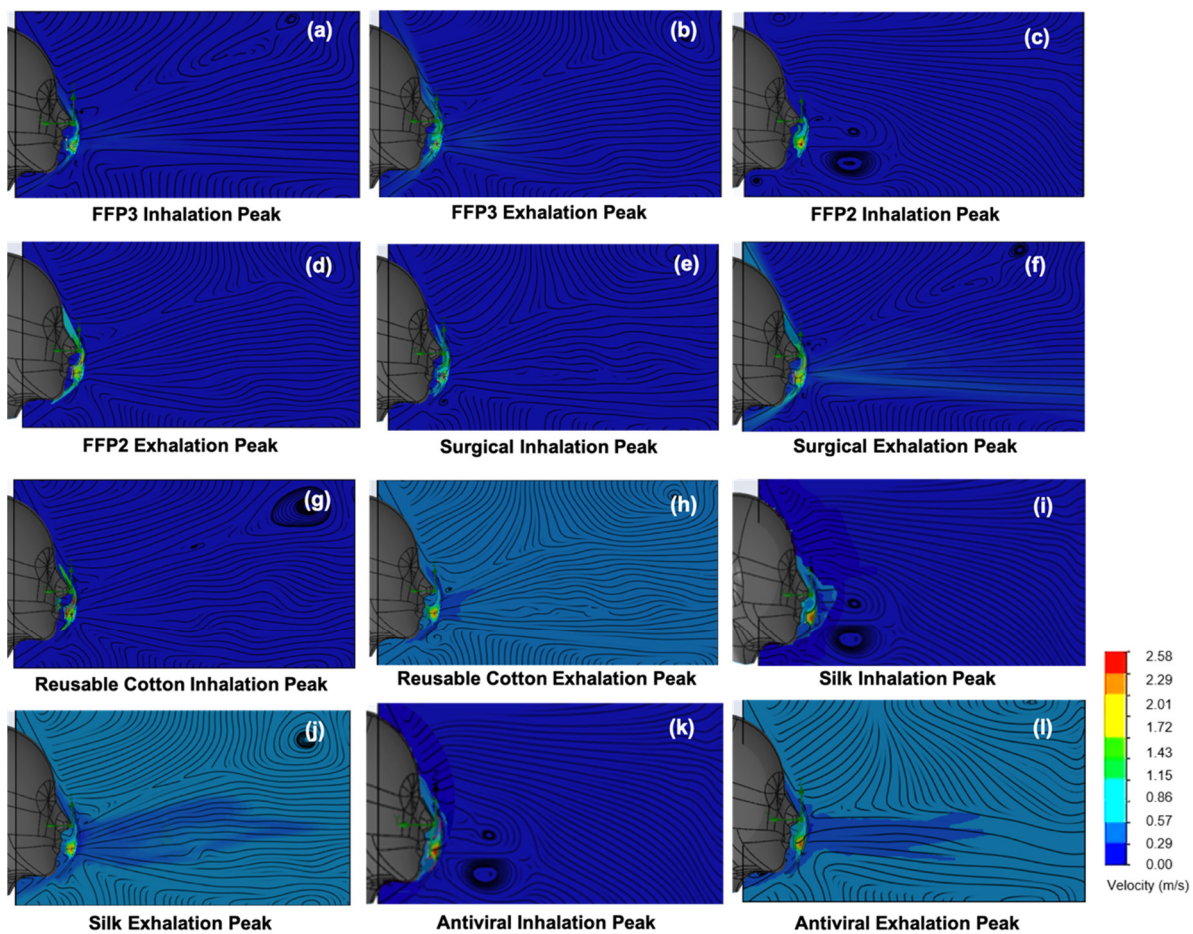


Figure 7. Air flow velocity distribution for the six different face masks during a breathing cycle at two time points, inhalation peak (at 3 s) and exhalation peak (at 1 s). Results are shown for FFP3 during the (a) inhalation and (b) exhalation peaks, FFP2 during the (c) inhalation and (d) exhalation peaks, surgical during the (e) inhalation and (f) exhalation peaks, reusable cotton during the (g) inhalation and (h) exhalation peaks, silk during the (i) inhalation and (j) exhalation peaks, antiviral during the (k) inhalation and (l) exhalation peaks.

Figure 8 shows the simulation results for the temperature distribution inside the face mask while wearing it at the inhalation peak ($t_2 = 3$ s) and the exhalation peak ($t_1 = 1$ s) during the breathing cycle. As the temperature of the exhaled air is high, this can increase the temperature inside the mask, whereas during the inhalation phase, the temperature inside the mask remains almost the same. However, different face masks exhibit different behaviors. For instance, the simulations show low temperature fluctuations for the FFP3 (Figure 8a,b) and FFP2 (Figure 8c,d) during the inhalation (29 °C) and exhalation (32 °C) peaks. However, the temperature near the nose and the mouth regions inside the mask increases (red area, 31–33 °C). This means that these two types of face masks exhibit high resistance to air flow (high filtration efficiency) as most of the exhaled air remains inside the masks, thus increasing the temperature. These results are well-correlated with the velocity profiles shown above (Figure 7a–d). The Surgical (Figure 8e,f) and the Reusable Cotton masks (Figure 8g,h) show similar behaviors. The temperature rises inside the masks during the exhalation peak, particularly around the mouth and nose areas. But, despite the temperature increases, there is no red area inside either mask (high-temperature regions), demonstrating less air flow resistance compared to the FFP3 and FFP2.

During the exhalation peak, both the silk (Figure 8i,j) and antiviral masks (Figure 8k,l) show a high-temperature area inside the mask. The increased temperature extends throughout the masks (red regions, 30–33 °C). This means that the resistance to air flow in these

two types of masks is low compared to *Surgical* and *Reusable Cotton*. This also means less resistance to the air flow velocity distribution (Figure 7j,l) during the exhalation phase. Overall, the results obtained from the simulations are consistent when compared to the data in Tables 2 and 3, indicating the high filtration efficiency of *FFP3* and *FFP2* in accordance with the standard EN 149 [31].

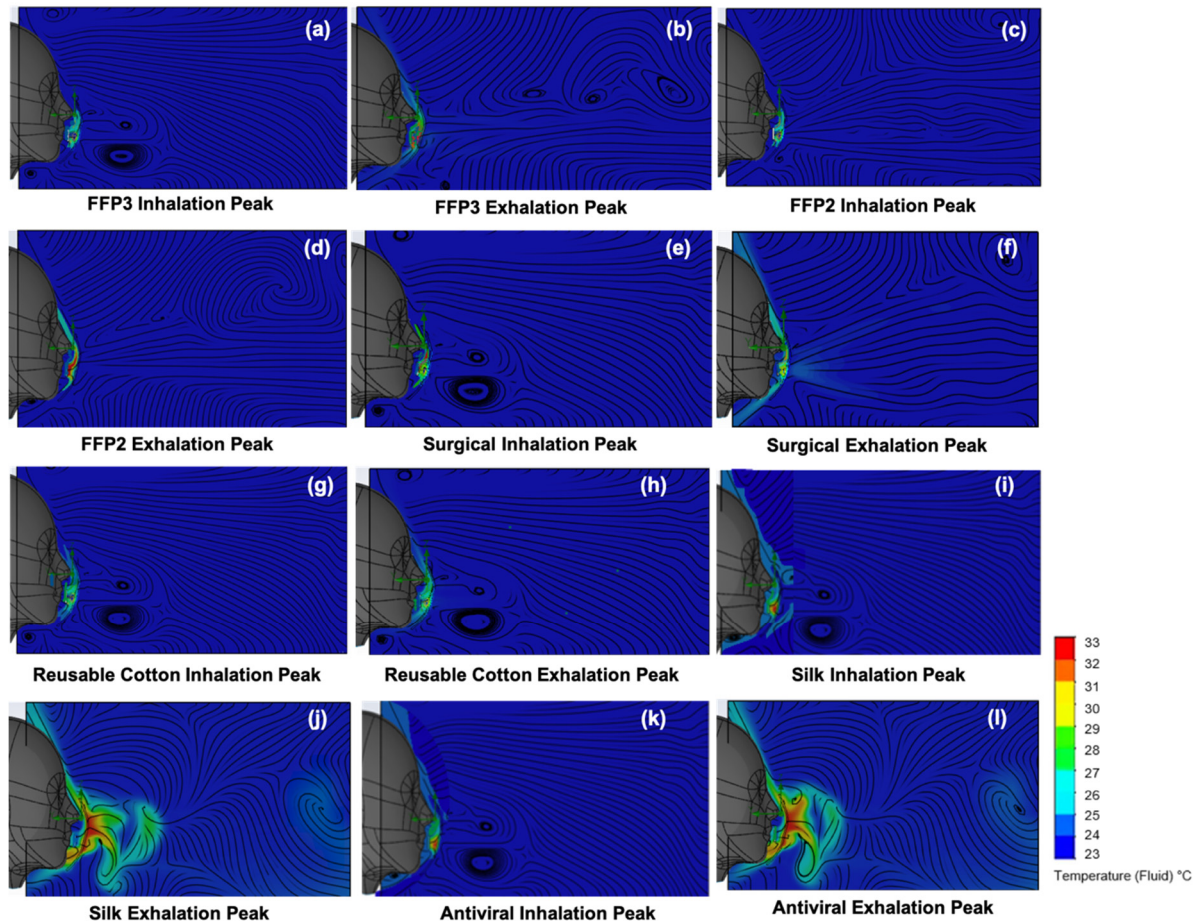


Figure 8. Time-dependent temperature distribution for all the six face masks during a breathing cycle at two-time points, inhalation peak (at 3 s) and exhalation peak (at 1 s). Results are displayed for *FFP3* during the (a) inhalation and (b) exhalation peaks, *FFP2* during the (c) inhalation and (d) exhalation peaks, *surgical* during the (e) inhalation and (f) exhalation peaks, *reusable cotton* during the (g) inhalation and (h) exhalation peaks, *silk* during the (i) inhalation and (j) exhalation peaks, *antiviral* during the (k) inhalation and (l) exhalation peaks.

4. Conclusions

This study evaluated the filtering and transmissibility properties of face mask layers individually and in combination using experimental data and mathematical analyses that provided velocity profiles and filtration efficiency. Air flow velocity measurement before and after passage through the edge-sealed masks has established their filtration efficiencies. These have been assessed experimentally using an air duct mask container fitted with pitot tubes at entry and exit within the centre and edges of the rectangular air duct. The particle size and distribution within the fabric weave were assessed by SEM. The porosity and fiber diameter of six different face masks have been investigated. Of these, *Reusable Cotton* has the largest, and *FFP3* has the lowest pore size. *Antiviral* and *Silk* masks show comparable pore sizes equal to approximately twice the pore size of the *surgical* and *FFP2* masks. Fiber diameters lie in a narrow range; the greatest and lowest sizes apply to *Surgical* and *Silk* fibers, respectively. Twelve healthy volunteers recorded the temperature and

humidity for both the mask and their body temperature. The results indicated an increase in temperature and humidity while wearing the masks, with no clinically significant change in body temperature. The *FFP2* and *FFP3* masks showed the greatest filtration efficiencies, each being in excess of 95%, a feature of the multi-layered designs. The simulations showed that *FFP2* and *FFP3* masks gave higher filtering efficiencies for small particles (<5 µm). The velocity distribution simulations showed that all six face masks have a low air velocity (~0.8–1.4 m/s) inside the mask (within the nose and mouth). Moreover, the temperature distribution simulations revealed small variations during breathing transmission. This study has provided information on an effective medical face mask design for the control and prevention of the spread of infectious diseases in the most common settings.

Author Contributions: Conceptualization, M.R. and D.R.; data curation, M.R. and D.R.; formal analysis, M.R. and D.R.; methodology, M.R., D.R., and F.P.; software, F.P.; supervision, M.R. and D.R.; validation, M.R., D.R., and S.H.; writing—original draft, M.R., D.R., and F.P.; writing—review & editing, M.R., D.R., and S.H. All authors have read and agreed to the published version of the manuscript.

Funding: No funding was received for conducting this study.

Institutional Review Board Statement: This study, conducted in accordance with established ethical guidelines and involving twelve healthy human volunteers, received ethical approval from the Brunel University Research Ethics Committee under the reference number 46938-MHR-Feb/2024-49825-3 (8 February 2024).

Informed Consent Statement: Informed consent was obtained from all participants. Additionally, parental consent was obtained for participants under 18, ensuring compliance with all relevant regulations.

Data Availability Statement: The data presented in this study are available on request from the corresponding author due to privacy and ethical restrictions.

Acknowledgments: We would like to thank Kevin Robinson and Paul Barrett for their technical help during the design process. The Mechanical Department of Brunel University London supplied the test facilities. The volunteers are thanked for their participation in this research activity.

Conflicts of Interest: The authors declare no conflicts of interest. However, reproduction or commercial use of this work is not permitted without prior written consent from the authors.

Abbreviations

Surgical	Medical-grade IIR surgical
Silk	Pure mulberry folded silk
FFP2	Filtering face piece 2
FFP3	Filtering face piece 3
F	Filtration efficiency
CFD	Computational fluid dynamics
SEM	Scanning electron microscopy

References

1. Dargahi, A.; Jeddi, F.; Ghobadi, H.; Vosoughi, M.; Karami, C.; Sarailoo, M.; Hadisi, A.; Mokhtari, S.A.; Haghighi, S.B.; Sadeghi, H.; et al. Evaluation of masks' internal and external surfaces used by health care workers and patients in coronavirus-2 (SARS-CoV-2) wards. *Environ. Res.* **2021**, *196*, 110948. [[CrossRef](#)] [[PubMed](#)]
2. Jayaweera, M.; Perera, H.; Gunawardana, B.; Manatunge, J. Transmission of COVID-19 virus by droplets and aerosols: A critical review on the unresolved dichotomy. *Environ. Res.* **2020**, *188*, 109819. [[CrossRef](#)] [[PubMed](#)]
3. Facciola, A.; Laganà, P.; Caruso, G. The COVID-19 pandemic and its implications on the environment. *Environ. Res.* **2021**, *201*, 111648. [[CrossRef](#)] [[PubMed](#)]
4. McDonald, F.; Horwell, C.J.; Wecker, R.; Dominelli, L.; Loh, M.; Kamanyire, R.; Ugarte, C. Facemask use for community protection from air pollution disasters: An ethical overview and framework to guide agency decision making. *Int. J. Disaster Risk Reduct.* **2020**, *43*, 101376. [[CrossRef](#)]

5. Cheng, V.C.; Wong, S.C.; Chuang, V.W.; So, S.Y.; Chen, J.H.; Sridhar, S.; To, K.K.; Chan, J.F.; Hung, I.F.; Ho, P.L.; et al. The role of community-wide wearing of face mask for control of coronavirus disease 2019 (COVID-19) epidemic due to SARS-CoV-2. *J. Infect.* **2020**, *81*, 107–114. [[CrossRef](#)] [[PubMed](#)]
6. Burnett, R.; Chen, H.; Szyszkowicz, M.; Fann, N.; Hubbell, B.; Pope III, C.A.; Apte, J.S.; Brauer, M.; Cohen, A.; Weichenthal, S.; et al. Global estimates of mortality associated with long-term exposure to outdoor fine particulate matter. *Proc. Natl. Acad. Sci. USA* **2018**, *115*, 9592–9597. [[CrossRef](#)]
7. Tcharkhtchi, A.; Abbasnezhad, N.; Seydani, M.Z.; Zirak, N.; Farzaneh, S.; Shirinbayan, M. An overview of filtration efficiency through the masks: Mechanisms of the aerosols penetration. *Bioact. Mater.* **2021**, *6*, 106–122. [[CrossRef](#)] [[PubMed](#)]
8. World Health Organization (WHO) Coronavirus (COVID-19). Available online: <https://data.who.int/dashboards/covid19/cases> (accessed on 26 May 2024).
9. Prather, K.A.; Wang, C.C.; Schooley, R.T. Reducing transmission of SARS-CoV-2. *Science* **2020**, *368*, 1422–1424. [[CrossRef](#)] [[PubMed](#)]
10. Hewawaduge, C.; Senevirathne, A.; Jawalagatti, V.; Kim, J.W.; Lee, J.H. Copper-impregnated three-layer mask efficiently inactivates SARS-CoV2. *Environ. Res.* **2021**, *196*, 110947. [[CrossRef](#)]
11. Zhang, S.; Liu, H.; Tang, N.; Zhou, S.; Yu, J.; Ding, B. Spider-web-inspired PM0. 3 filters based on self-sustained electrostatic nanostructured networks. *Adv. Mater.* **2020**, *32*, e2002361. [[CrossRef](#)]
12. Kang, D.H.; Kim, N.K.; Kang, H.W. Electrostatic charge retention in PVDF nanofiber-nylon mesh multilayer structure for effective fine particulate matter filtration for face masks. *Polymers* **2021**, *13*, 3235. [[CrossRef](#)] [[PubMed](#)]
13. Victor, F.S.; Kugarajah, V.; Bangaru, M.; Ranjan, S.; Dharmalingam, S. Electrospun nanofibers of polyvinylidene fluoride incorporated with titanium nanotubes for purifying air with bacterial contamination. *Environ. Sci. Pollut. Res. Int.* **2021**, *28*, 37520–37533. [[CrossRef](#)] [[PubMed](#)]
14. Bayersdorfer, J.; Giboney, S.; Martin, R.; Moore, A.; Bartles, R. Novel manufacturing of simple masks in response to international shortages: Bacterial and particulate filtration efficiency testing. *Am. J. Infect. Control.* **2020**, *48*, 1543–1545. [[CrossRef](#)] [[PubMed](#)]
15. Podgórski, A.; Bałazy, A.; Gradoń, L. Application of nanofibers to improve the filtration efficiency of the most penetrating aerosol particles in fibrous filters. *Chem. Eng. Sci.* **2006**, *61*, 6804–6815. [[CrossRef](#)]
16. Zangmeister, C.D.; Radney, J.G.; Vicenzi, E.P.; Weaver, J.L. Filtration efficiencies of nanoscale aerosol by cloth mask materials used to slow the spread of SARS-CoV-2. *ACS Nano* **2020**, *14*, 9188–9200. [[CrossRef](#)] [[PubMed](#)]
17. Richardson, A.W.; Eshbaugh, J.P.; Hofacre, K.C.; Gardner, P.D. *Respirator Filter Efficiency Testing against Particulate and Biological Aerosols under Moderate to High Flow Rates*; Battelle Memorial Institute: Columbus, OH, USA, 2006.
18. Guha, S.; McCaffrey, B.; Hariharan, P.; Myers, M.R. Quantification of leakage of sub-micron aerosols through surgical masks and facemasks for pediatric use. *J. Occup. Environ. Hyg.* **2017**, *14*, 214–223. [[CrossRef](#)] [[PubMed](#)]
19. Aydin, O.; Emon, B.; Cheng, S.; Hong, L.; Chamorro, L.P.; Saif, M.T. Performance of fabrics for home-made masks against the spread of COVID-19 through droplets: A quantitative mechanistic study. *Extreme Mech. Lett.* **2020**, *40*, 100924. [[CrossRef](#)]
20. Wilson, N.; Corbett, S.; Tovey, E. Airborne transmission of COVID-19. *BMJ* **2020**, *20*, 370. [[CrossRef](#)]
21. Konda, A.; Prakash, A.; Moss, G.A.; Schmoldt, M.; Grant, G.D.; Guha, S. Aerosol filtration efficiency of common fabrics used in respiratory cloth masks. *ACS Nano* **2020**, *14*, 6339–6347. [[CrossRef](#)]
22. Schilling, K.; Gentner, D.R.; Wilen, L.; Medina, A.; Buehler, C.; Perez-Lorenzo, L.J.; Pollitt, K.J.; Bergemann, R.; Bernardo, N.; Peccia, J.; et al. An accessible method for screening aerosol filtration identifies poor-performing commercial masks and respirators. *J. Expo. Sci. Environ. Epidemiol.* **2021**, *31*, 943–952. [[CrossRef](#)]
23. Drewnick, F.; Pikkmann, J.; Fachinger, F.; Moormann, L.; Sprang, F.; Borrmann, S. Aerosol filtration efficiency of household materials for homemade face masks: Influence of material properties, particle size, particle electrical charge, face velocity, and leaks. *Aerosol Sci. Technol.* **2021**, *55*, 63–79. [[CrossRef](#)]
24. Kwong, L.H.; Wilson, R.; Kumar, S.; Crider, Y.S.; Reyes Sanchez, Y.; Rempel, D.; Pillarisetti, A. Review of the breathability and filtration efficiency of common household materials for face masks. *ACS Nano* **2021**, *15*, 5904–5924. [[CrossRef](#)] [[PubMed](#)]
25. Hinds, W.C.; Zhu, Y. *Aerosol Technology*, 3rd ed.; John Wiley & Sons, Inc.: New York City, NY, USA, 2022.
26. Corbin, J.C.; Smallwood, G.J.; Leroux, I.D.; Olliaee, J.N.; Liu, F.; Sipkens, T.A.; Gree, R.G.; Murnaghan, N.F.; Koukoulas, T.; Lobo, P. Systematic experimental comparison of particle filtration efficiency test methods for commercial respirators and face masks. *Sci. Rep.* **2021**, *11*, 21979. [[CrossRef](#)] [[PubMed](#)]
27. Zhao, M.; Liao, L.; Xiao, W.; Yu, X.; Wang, H.; Wang, Q.; Lin, Y.L.; Kilinc-Balci, F.S.; Price, A.; Chu, L.; et al. Household materials selection for homemade cloth face coverings and their filtration efficiency enhancement with triboelectric charging. *ACS Nano Lett.* **2020**, *20*, 5544–5552. [[CrossRef](#)] [[PubMed](#)]
28. Allison, A.L.; Ambrose-Dempster, E.; Bawn, M.; Casas Arredondo, M.; Chau, C.; Chandler, K.; Dobrijevic, D.; Domenech Aparisi, T.; Hailes, H.C.; Lettieri, P.; et al. The impact and effectiveness of the general public wearing masks to reduce the spread of pandemics in the UK: A multidisciplinary comparison of single-use masks versus reusable face masks. *UCL Open Environ.* **2021**, *3*, e022. [[CrossRef](#)] [[PubMed](#)]
29. O’Kelly, E.; Pirog, S.; Ward, J.; Clarkson, P.J. Ability of fabric face mask materials to filter ultrafine particles at coughing velocity. *BMJ Open.* **2020**, *10*, e039424. [[CrossRef](#)] [[PubMed](#)]
30. Matsuyama, S.; Nao, N.; Shirato, K.; Kawase, M.; Saito, S.; Takayama, I.; Nagata, N.; Sekizuka, T.; Katoh, H.; Kato, F.; et al. Enhanced isolation of SARS-CoV-2 by TMPRSS2-expressing cells. *Proc. Natl. Acad. Sci. USA* **2020**, *117*, 7001–7003. [[CrossRef](#)] [[PubMed](#)]

31. EN 149:2001+A1:2009 (E); Respiratory Protective Devices—Filtering Half Masks to Protect against Particles—Requirements, Testing, Marking. European Committee for Standardization (CEN): Brussels, Belgium, 2009.
32. Lewitt, E.H. *Hydraulics and Fluid Mechanics: A Text-Book Covering the Syllabuses of the B. Sc.(Eng.), ICE and I. Mech. E. Examinations in this Subject*, 10th ed.; Pitman & Sons Ltd.: London, UK, 1970.
33. Sanchez, E. Filtration Efficiency of Surgical Masks. USF Tampa Graduate Theses and Dissertations. 2010. Available online: <https://scholarcommons.usf.edu/etd/1760> (accessed on 26 May 2024).
34. Lei, Z.; Yang, J.; Zhuang, Z.; Roberge, R. Simulation and evaluation of respirator face seal leaks using computational fluid dynamics and infrared imaging. *Ann. Occup. Hyg.* **2013**, *57*, 493–506. [[CrossRef](#)] [[PubMed](#)]
35. Zhang, X.; Li, H.; Shen, S.; Cai, M. Investigation of the flow-field in the upper respiratory system when wearing N95 filtering facepiece respirator. *J. Occup. Environ. Hyg.* **2016**, *13*, 372–382. [[CrossRef](#)]
36. Rasekh, M.; Pisapia, F.; Howkins, A.; Rees, D. Materials analysis and image-based modelling of transmissibility and strain behaviour in approved face mask microstructures. *Sci. Rep.* **2022**, *12*, 17361. [[CrossRef](#)]
37. Memarzadeh, F. Improved strategy to control aerosol-transmitted infections in a hospital suite. *ASHRAE Trans.* **2011**, *117*, 1–10.
38. Kowalski, W.J.; Bahnfleth, W.P. Airborne respiratory diseases and mechanical systems for control of microbes. *HPAC Heat. Pip. Air Cond.* **1998**, *7*, 11.
39. Courtney, J.M.; Bax, A. Hydrating the respiratory tract: An alternative explanation why masks lower severity of COVID-19. *Biophys. J.* **2021**, *120*, 994–1000. [[CrossRef](#)]
40. Walker, F.C.; Sridhar, P.R.; Baldrige, M.T. Differential roles of interferons in innate responses to mucosal viral infections. *Trends Immunol.* **2021**, *42*, 1009–1023. [[CrossRef](#)]
41. Cherrie, J.W.; Wang, S.; Mueller, W.; Wendelboe-Nelson, C.; Loh, M. In-mask temperature and humidity can validate respirator wear-time and indicate lung health status. *J. Expo. Sci. Environ. Epidemiol.* **2019**, *29*, 578–583. [[CrossRef](#)]
42. Popov, T.A.; Kralimarkova, T.Z.; Dimitrov, V.D. Measurement of exhaled breath temperature in science and clinical practice. *Breathe* **2012**, *8*, 186–192. [[CrossRef](#)]
43. Grinshpun, S.A.; Haruta, H.; Eninger, R.M.; Reponen, T.; McKay, R.T.; Lee, S.A. Performance of an N95 filtering facepiece particulate respirator and a surgical mask during human breathing: Two pathways for particle penetration. *J. Occup. Environ. Hyg.* **2009**, *6*, 593–603. [[CrossRef](#)] [[PubMed](#)]
44. Gupta, J.K.; Lin, C.H.; Chen, Q. Characterizing exhaled airflow from breathing and talking. *Indoor Air* **2010**, *20*, 31–39. [[CrossRef](#)] [[PubMed](#)]
45. Lee, H.C.; Wahab, A.K. Performance of different turbulence models in predicting flow kinematics around an open offshore intake. *SN Appl. Sci.* **2019**, *1*, 1266. [[CrossRef](#)]
46. Bahmanzadeh, H.; Abouali, O.; Faramarzi, M.; Ahmadi, G. Numerical simulation of airflow and micro-particle deposition in human nasal airway pre-and post-virtual sphenoidotomy surgery. *Comput. Biol. Med.* **2015**, *61*, 8–18. [[CrossRef](#)]
47. Napoli, N.J.; Rodrigues, V.R.; Davenport, P.W. Characterizing and modeling breathing dynamics: Flow rate, rhythm, period, and frequency. *Front. Physiol.* **2022**, *12*, 2305. [[CrossRef](#)] [[PubMed](#)]
48. Russo, J.S.; Khalifa, E. Computational study of breathing methods for inhalation exposure. *HVAC&R Res.* **2011**, *17*, 419–431. [[CrossRef](#)]
49. Rofail, P.; Afify, R.; El-Gamal, H. Computational and experimental investigations of a novel reusable face mask for treating sinusitis disease. *Ain Shams Eng. J.* **2021**, *12*, 2965–2979. [[CrossRef](#)]
50. Zhang, X.; Li, H.; Shen, S.; Rao, Y.; Chen, F. An Improved FFR Design with a Ventilation Fan: CFD Simulation and Validation. *PLoS ONE* **2016**, *11*, e0159848. [[CrossRef](#)]

Disclaimer/Publisher’s Note: The statements, opinions and data contained in all publications are solely those of the individual author(s) and contributor(s) and not of MDPI and/or the editor(s). MDPI and/or the editor(s) disclaim responsibility for any injury to people or property resulting from any ideas, methods, instructions or products referred to in the content.